Title
Simultaneous imaging of radiation-induced cerebral microbleeds, arteries and veins, using a multiple gradient echo sequence at 7 Tesla.

Permalink

Journal

ISSN

Authors
Bian, Wei
Banerjee, Suchandrima
Kelly, Douglas AC
et al.

Publication Date

DOI

Peer reviewed

Simultaneous Imaging of Radiation-Induced Cerebral Microbleeds, Arteries and Veins, Using a Multiple Gradient Echo Sequence at 7 Tesla

Wei Bian, MS[1,2], **Suchandrima Banerjee, PhD**[3], **Douglas A.C. Kelly, PhD**[4], **Christopher P. Hess, MD, PhD**[2], **Peder E.Z. Larson, PhD**[1,2], **Susan M. Chang, MD**[5], **Sarah J. Nelson, PhD**[1,2,6], and **Janine M. Lupo, PhD**[2,*]

[1]The UC Berkeley-UCSF Graduate Program in Bioengineering, University of California San Francisco, San Francisco, California, USA

[2]Department of Radiology and Biomedical Imaging, University of California San Francisco, San Francisco, California, USA

[3]Global Applied Science Laboratory, GE Healthcare, Menlo Park, California, USA

[4]Global Applied Science Laboratory, GE Healthcare, San Francisco, California, USA

[5]Department of Neurological Surgery, University of California San Francisco, San Francisco, California, USA

[6]Department of Bioengineering and Therapeutic Sciences, University of California San Francisco, San Francisco, California, USA

Abstract

Background—The purpose of this study was to implement and evaluate the utility of a multi-echo sequence at 7 Tesla (T) for simultaneous time-of-flight (TOF) MR-angiography (MRA) and susceptibility-weighted imaging (SWI) of radiation-induced cerebral microbleeds (CMBs), intracranial arteries, and veins.

Methods—A four-echo gradient-echo sequence was implemented on a 7T scanner. The first echo was used to create TOF-MRA images, while the remaining echoes were combined to visualize CMBs and veins on SWI images. The sequence was evaluated on eight brain tumor patients with known radiation-induced CMBs. Single-echo images were also acquired to visually and quantitatively compare the contrast-to-noise ratio (CNR) of small- and intermediate-vessels between acquisitions. The number of CMBs detected with each acquisition was also quantified. Statistical significance was determined using a Wilcoxon signed-rank test.

Results—Compared with the single-echo sequences, the CNR of small and intermediate arteries increased 7.6% ($P < 0.03$) and 9.5% ($P = 0.06$), respectively, while the CNR of small and intermediate veins were not statistically different between sequences ($P = 0.95$ and $P = 0.46$,

---

[*]Address reprint requests to: J.M.L., Byers Hall UCSF, Box 2532, 1700 4th Street, Suite 303, San Francisco, CA 94158. ; Email: janine.lupo@ucsf.edu.

respectively). However, these differences were not discernible by visual inspection. Also the multi-echo sequence detected 18.3% more CMBs ($P < 0.008$) due to higher slice resolution.

Conclusion—The proposed 7T multi-echo sequence depicts arteries, veins, and CMBs on a single image to facilitate quantitative evaluation of radiation-induced vascular injury.

Radiation Therapy (RT) is a widely used treatment in the management of patients with malignant brain tumors.[1] It is often used either in conjunction with chemotherapy after surgical resection to reduce residual tumor burden or alone in surgically inaccessible tumors.[1] Despite its effectiveness and recent modern advances to constrain dose distribution more effectively to the tumor, collateral injury to normal brain tissue is always present and includes coagulative necrosis, white matter demyelization, cortical atrophy, and endothelial proliferation.[2] RT is also correlated with the development of vascular abnormalities including cavernous malformations,[3] moyamoya-like progressive steno-occlusive disease,[4] accelerated atherosclerosis, and other forms of large vessel arteriopathy.[5] At the microvascular level, histopathological analyses reveal a spectrum of radiation injury that includes endothelial disruption, fibrinoid necrosis, luminal narrowing, and occlusion, which leads to the formation of cerebral microbleeds (CMBs) in otherwise normal-appearing brain tissue.[6,7] These hemosiderin-containing deposits begin to appear approximately two years post-RT and continue to increase in number over time.[8–11] More recent studies have demonstrated a correlation between the number of CMBs and the dose and the target volume defined for radiation therapy,[10,11] pointing to the potential use of these lesions as a surrogate quantitative marker of radiation injury. While the origin of CMBs has not been completely defined, ionizing radiation is known to have a greater effect on smaller caliber vasculature and is more likely to damage arteries than veins.[6] A strategy to noninvasively image arteries and veins simultaneously, and to assess the spatial distribution of CMBs relative to these structures would help to establish a relationship between CMB formation and underlying vascular pathology, and aid in clinical and basic science studies of CMB that arise in cerebral amyloid angiopathy (CAA),[12] stroke,[13] Alzheimer's disease,[14] traumatic brain injury (TBI),[15] mild cognitive impairment,[16] and dementia.[17]

CMBs can be observed noninvasively on MR images using T2*-weighted gradient echo sequences as small hypointense lesions, often with spherical shape.[18] These imaging features are enhanced by susceptibility-weighted imaging (SWI), an MR imaging technique that is more sensitive to CMBs than conventional T2*-weighted imaging [8–10,19] and permits accurate visualization of intracranial veins as hypointense due to the presence of iron-containing deoxyhemoglobin.[20] In contradistinction, arterial contrast in three-dimensional (3D) time-of-flight (TOF) MR angiography (MRA) is determined by flow-related enhancement and background suppression.[21] While the utility of these sequences for characterizing CMBs [8–10,19] and intracranial vessels[20–24] has been demonstrated, accounting for prescanning, the combined time spent on the two separate sequences can be 15 to 20 min. Also, accurate registration is nearly impossible to attain due to the lack of both anatomical contrast and structural similarity between the TOF-MRA and SWI, in addition to the blurring of sub-millimeter CMBs and microvasculature after the interpolation step of the registration. Thus, a combined MRA-SWI sequence using multiple gradient echoes can not only reduce scan time but also obviate the need for image coregistration, which would

benefit our understanding of CMB formation by providing metrics that reflect the interaction among vascular structures that are not confounded by inaccuracies in the coregistration.

The ability to obtain a simultaneous acquisition of 3D TOF-MRA and SWI in a single imaging sequence with multiple echoes has been recently demonstrated in a normal volunteer at 3 Tesla (T).[25] The elevated SNR, heightened background suppression for TOF-MRA, and amplified susceptibility contrast for SWI available at 7T demonstrates the potential of this platform to provide excellent delineation of both CMBs and microvasculature.[8,22] While previous studies have demonstrated the capability of implementing a dual- or multi-echo acquisition on normal volunteers,[25–28] there have been no efforts at simultaneously optimizing contrast of CMBs and microvasculature, creating combined SWI images from multiple echoes, reconstruction and processing improvements, or clinical evaluation. The purpose of this study was to design a 7T multi-echo sequence and SWI reconstruction pipeline using data from multiple echoes, and assess resulting image quality by comparing it with that of separate TOF-MRA and SWI acquisitions. By using the sequence, we aim to obtain high-resolution vascular images for the simultaneous depiction of arteries, veins, and CMBs in patients with brain tumors treated with prior radiation therapy.

Method and Materials

Sequence Design

A multi-echo sequence was created by adding three additional echoes to a single-echo, multi-slab 3D spoiled gradient recalled (SPGR) echo sequence with TOF capabilities on a GE 7T system (GE Healthcare, Waukesha, WI) equipped with a 32-channel phased array receive coil insert situated within a volume transmit coil (Nova Medical, Wilmington, MA). The first echo was used to create TOF-MRA images, while the remaining three echoes were combined to generate a composite SWI image. The sequence diagram of the final empirically optimized acquisition scheme is shown in Figure 1. Because adequate background suppression and heightened contrast of arteries on the TOF-MRA images requires minimizing the echo time (TE) of the first echo and overall repetition time (TR), flow compensation was performed only in the readout direction and all echoes were partially acquired with a 65% sampling coverage. This resulted in a TE1/TE2/TE3/TE4 of 2.7/10.5/13.2/20.9 ms and a TR of 40ms when using a bandwidth of 41.67 kHz, in-plane matrix of 512×384, and FOV of 24 cm. A small flip angle of 25 ° was used for excitation and a multiple overlapping thin-slab acquisition (MOTSA),[24] an approach that is widely used for TOF-MRA, was applied to all four echoes. Three slabs with thirty-six 1-mm-thick slices and 12 slices of overlap were used to minimize signal saturation for the TOF-MRA images from the first echo while maintaining a large enough 3D volume to achieve adequate SNR for SWI image obtained from the later echoes. The acquisition was accelerated in the phase encoding direction with an autocalibrating partially parallel imaging strategy that used an acceleration factor of 3 and 16 auto-calibrating lines, resulting in a total acquisition time of 10.6 min.

Image Reconstruction

The raw complex *k*-space data from all 32 coils were transferred off-line to a Linux workstation, where postprocessing was performed using in-house programs developed with MATLAB 7.0 software (MathWorks, Natick, MA). Our processing pipeline for reconstruction and combination of multi-echo, multi-channel data is illustrated in Figure 2. For each individual coil, missing phase-encoding lines were recovered using an autocalibrating parallel imaging reconstruction method: auto-calibrating reconstruction for Cartesian sampling (ARC).[29] For reconstruction of magnitude images at each echo, all partially-acquired *k*-space echoes were recovered to their full extent by projection onto convex sets (POCS).[30] The full FOV 512×384 *k*-space data from all echoes were then zero-padded out in the phase-encoding direction to create a 512×512 matrix before taking the inverse Fourier transform. Magnitude images from each coil were combined using the root sum of squares [31] and skull stripped using FMRIB Software Library's (FSL) Brain Extraction Tool (BET).[32] The final magnitude images from the first echo were used for TOF-MRA while those from the final three echoes were used for subsequent SWI processing described as follows.

During SWI processing, the data from the final three echoes were, first, processed individually before a composite SWI image was created (Fig. 2). To generate high-pass filtered phase images for each coil, the complex *k*-space data after ARC reconstruction from echoes 2–4 were zero-filled in the frequency-encoding direction, followed by homodyne filtering with Hanning filter sizes of 72, 88, and 104 for the 2nd, 3rd, and 4th echoes, respectively. These filter sizes were empirically determined for each TE to preserve local contrast while removing macroscopic background phase wraps. The high-pass filtered phase images from each coil were combined by weighted sum (weighted by the square of corresponding magnitude intensity). The phase images from echoes 2~4 was then averaged to produce a mean phase image, from which a negative phase mask was created by linearly scaling negative phase values between zero and one and setting positive phase values to one. This mean phase image was later examined to confirm the absence of calcification in these lesions, as paramagnetic microbleeds are hypointense on both SWI and phase images while diamagnetic calcifying lesions appear hyperintense on phase images even though they are hypointense on SWI images. The mean magnitude image from the three echoes was also produced and multiplied with the phase mask 4 times to generate the final composite SWI image.

Clinical Evaluation

The proposed sequence was evaluated on eight patients (four males and four females with a mean age of 45.2 years and a range from 29.8 to 67.1 years) who were specifically recruited for this study because of the presence of multiple confirmed CMBs due to prior external beam radiation therapy of a resected glioma. The time between the 7T imaging examination and start of radiation ranged from 3 to 15 years. The study was approved by our institutional Committee for Human Research, and written informed consent was obtained from all patients. Conventional single-echo TOF-MRA and SWI sequences with the same acceleration, FOV, image matrix, flip angle, and coverage were scanned in addition to the

combined multi-echo sequence on all patients. The other parameters used for each sequence are listed in Table 1.

Data Analysis

To evaluate the quality of the depiction of arteries, veins, and CMBs in images generated from the combined multi-echo sequence, maximum and minimum intensity projections (maxIP and minIP) through 8-mm-thick slices were created for all TOF-MRA and SWI images, respectively. These projected images were used to both count the number of CMBs detected on SWI images and quantify the contrast-to-noise ratio (CNR) of *small-* (diameter 1 mm) and *intermediate-* (1 mm < diameter 2 mm) sized vessels. CMBs were defined as round, hypointense foci with diameters less than 5 mm on consecutive slices. An automated detection algorithm [33] that was highly sensitive to radiation-induced CMBs on minIP SWI images was used to identify CMBs in approximately 1 min. The algorithm used geometric features such as shape, area, and circularity to distinguish potential CMBs from other sources of hypointense signal, including linear vessels and susceptibility artifacts. The output from the automatic detection was then independently inspected by two raters (W.B. and J.M.L.) in random order to remove any remaining false positives, add any CMBs that were missed by the automated detection, and count the identified CMBs. The raters had 7 and 11 years experience, respectively, in brain tumor imaging and, more specifically, 4 and 6 years identifying and evaluating CMB under the guidance of a board certified neuroradiologist (C.P.H.), who also visually evaluated the overall image quality of arteries and veins on images from both single- and multi-echo sequences. The mean phase images were also examined by W.B. and J.M.L. to verify that all identified CMBs were not due to the presence of calcification, which would appear hyperintense on phase images because calcium is diamagnetic.[8]

The inter-rater agreement of the CMB counting was measured by calculating an intraclass correlation coefficient (ICC) based on absolute agreement. The final CMB counts that were obtained from each rater were averaged to quantify the number of true CMBs for each patient. CNR was calculated from 10 regions of interest (ROIs) for each size vessel on both the TOF-MRA and SWI images. Each vessel segment selected was carefully matched in size and length between the single- and multi-echo sequences to minimize any effects of motion or partial voluming between scans and spaced to span the entire supra-tentorial brain coverage to minimize any bias from spatial variations in contrast due to the parallel reconstruction. This resulted in 40 total vessel segments for each patient. ROIs of background brain parenchyma were generated by first dilating each vessel ROI (with a kernel size of .5 mm and 1 mm for small and intermediate vessels, respectively) and then subtracting the vessel ROI from the dilated ROI. Examples of vessel and background ROIs are illustrated in Figure 3. Noise was estimated from the standard deviation of a homogeneous region of corpus callosum for both the TOF-MRA and SWI according to Denk and Rauscher.[34] CNR was calculated as the difference in the median values between the vessel and background ROIs divided by the noise. The 10 CNR values from each vessel type were then averaged for each patient. A Wilcoxon signed-rank test was used to test for significant differences in the averaged CNR and the number of CMBs between image acquisitions.

Results

The benefit of combining data from echoes 2–4 in the creation of a composite SWI image compared with using data from a single echo time is illustrated in Figure 4A. SNR was improved for the combined composite SWI image compared with the SWI image generated from echo 3 (whose TE was similar to that of the single-echo SWI sequence), as evident by a more homogeneous appearance of the ventricles on the composite image due to the reduction of noise. Plots of average CNR for both *small* and *intermediate* veins on minIP SWI images from echo 3 and all echoes combined for all eight patients are shown in Figure 4B. Combining the 2nd–4th echoes of the multi-echo sequence resulted in an average CNR that was 52.2% and 45.0% higher than those measured on the minIP SWI images from the third echo only for *small* and *intermediate* veins, respectively (both statistically significant with $P < 0.008$).

Visually, the overall image quality was comparable between the single- and multi-echo sequences, with a slight degradation of background suppression on the TOF-MRA and higher noise level on the SWI images generated from the multi-echo sequence. Both *small* and *intermediate* veins were similarly depicted on the single- and multi-echo sequences. In addition, single-echo SWI was able to better delineate large draining veins, while smaller veins and CMBs were observed on the multi-echo SWI images, primarily due to its higher slice resolution. A typical example of this is shown in Figure 5A. On the other hand, all arteries appeared similarly on the multi-echo and single-echo TOF-MRA despite the slightly worse background suppression of the multi-echo acquisition, due to the longer TR (Fig. 5B).

Figure 5C shows plots of average CNR for each type of vessel calculated from the multi- and single-echo sequences from all eight patients. On average, CNRs of *small* and *intermediate* veins were not significantly different between the single- and multi-echo SWI images (3% difference with $P = 0.95$ for *small* veins and 6.7% difference with $P = 0.46$ for *intermediate* veins). The average CNR of *small* and *intermediate* arteries on TOF-MRA increased 7.6% and 9.5%, respectively, for the multi-echo sequence compared with values obtained from the single-echo sequence. Although this difference was statistically significant for *small* arteries ($P < 0.03$), it did not reach significance for *intermediate* ones ($P = 0.06$).

Figure 6A displays an overlay of a thresholded slice of TOF-MRA (maxIP over 8 mm) on the minIP SWI image from the multi-echo sequence. From this overlay, it is apparent that some CMBs are clearly arising from venous vessels (as denoted by the pink dashed-box) while others appear to originate from arterioles (green dashed-box). Table 2 lists the number of CMBs detected from both sequences for each patient. None of the identified CMBs were found to be calcifications after visual inspection of the mean phase images. Both raters consistently detected more CMBs on the multi-echo minIP SWI images than on the single-echo minIP images ($P < 0.008$ for rater 1 and $P < 0.024$ for rater 2). The ICC between the two raters on CMB counting from all eight patients was 0.995 for both the single- and multi-echo images. Because the ICC calculation is heavily influenced by the number of CMBs and can be artificially elevated when the variability in CMB counts among patients is large, we repeated the calculation excluding the two patients who had more than 200 CMBs. This more reliable estimation of inter-rater agreement resulted in ICCs of 0.920 and 0.872 for the

single- and multi-echo images, respectively. When the CMB counts from both raters were averaged, the multi-echo sequence detected 18.3% more CMBs than the single echo minIP SWI image ($P < 0.008$), with 945.5 and 798.5 total CMBs identified, respectively. Each individual patient also had more CMBs identified on the multi-echo images. These additional CMBs were typically smaller in size as shown in Figure 6B.

Discussion

The heightened susceptibility contrast recently available with higher field strength scanners has greatly motivated the investigation of the clinical relevance of CMBs in neurological disorders such as CAA,[12] stroke,[13] Alzheimer's disease,[14] TBI,[15] and radiation injury.[8–11] The majority of prior MR imaging studies of CMBs have focused primarily on characterizing CMB properties such as number, size, and location, how the selection of imaging parameters affects these properties, and their relationship to neurocognitive decline.[8,19,35–37] Despite its implication in radiation injury and CMB formation, the spatial relationship between CMBs and surrounding microvasculature has received only limited attention. The ability to simultaneously visualize CMBs, arteries, and veins in direct spatial correspondence on one image will facilitate the quantification of metrics that reflect the interaction among these structures, greatly aiding in the characterization of the mechanism of radiation-induced vascular injury as well as understanding the role of CMB presence in other diseases.

Motivated by these desires, we implemented a multi-echo, multi-slab gradient echo sequence with parallel imaging capability at 7T in this study. The sequence was able to acquire 3D TOF-MRA and SWI simultaneously and provided comparable image quality to each individual single-echo sequence for the depiction of intracranial arteries, veins, and radiation-induced CMBs without the need for image registration. The additional flexibility in SWI processing with multiple echoes also allowed for thinner slices, which not only improved CMB detection even further, but also enhanced the contrast of smaller veins. With the same coverage as both single-echo sequences and twice the slice resolution of the single-echo SWI, the multi-echo sequence had an acquisition time that was less than the total acquisition time of two individual single-echo acquisitions and was comparable to that of previous studies.[26–29]

Successful implementation of a multi-echo sequence for 3D TOF-MRA and SWI required careful selection of imaging parameters to achieve adequate background suppression on TOF-MRA and reasonable SNR preservation on SWI. The requisite longer TR and thicker slabs for the SWI results in reduced background suppression and lower CNR for the TOF-MRA images, while the multi-slab, partial-echo acquisition with thinner slices necessary for TOF-MRA degrades the quality of SWI images. Because our aim was to image small intracranial vessels and CMBs, our first constraint was to maintain a minimum slice and slab thickness of 1 mm and 36 mm, respectively, which created a challenge in further optimization of other sequence parameters. Compared with previous studies that used comparable in-plane resolution,[25–28] our slice and slab thickness were at least 17% and 30% thinner, respectively. To achieve this desired resolution, a composite SWI image was created from three echoes to improve the degraded CNR of SWI images due to the thin slice/slab

thickness. Although the TR of the TOF-MRA mainly limited the number of additional echoes that could be incorporated, the addition of echoes at TEs over 22 ms would not have provided any further benefit to the composite SWI image because of the concomitant susceptibility distortions that occur at long TEs at 7T. Despite these tradeoffs, the combination of parameters chosen and modified SWI processing of the later echoes preserved the quality of both TOF-MRA and SWI images with good contrast.

Both *small* and *intermediate* arteries had a higher CNR on TOF-MRA from the multi-echo sequence. This can be explained by the thicker slab thickness and longer TR of the multi-echo sequence that increased the signal from both arteries and background tissue. Although the latter would lead to less efficient background suppression, the longer TR enhanced the in-flow effect of slowly flowing blood spins in small arteries, which further increased the signal from arteries. At the same time, because all other TOF-MRA acquisition parameters (i.e., resolution, bandwidth, TE, and sampling coverage) were kept constant between the multi- and single-echo sequences, their noise level should have been similar. Therefore, it is not surprising that a longer acquisition time for the multi-echo TOF-MRA resulted in a slightly higher CNR.

To explain the observed difference in CNR for veins, the image reconstruction/postprocessing strategy must also be taken into consideration in addition to the acquisition parameters of the two sequences. Compared with the single-echo SWI sequence, all individual echoes of the multi-echo sequence had half the slice thickness, 2.7 times higher bandwidth, 6.3 times shorter TR, and 35% less sampling coverage, resulting in the reduced CNR and SNR observed on the images obtained from echo 3. However, averaging magnitude and phase images from echoes 2–4 greatly improved CNR of veins in the composite minIP SWI image compared with minIP SWI images generated from the 3rd echo only. This result was similar to findings of previous studies that generated SWI images from data acquired at multiple echoes.[34,38–40] Because of this processing pipeline, the CNR of both *intermediate* and *small* veins from the composite multi-echo SWI images were not significantly different from values obtained from the conventional single-echo images. The improved CNR observed in extremely small vessels with the multi-echo sequence was likely due to the thinner slice thickness of the multi-echo sequence, which reduced partial voluming effects for these vessels. Likewise, the thinner slices also facilitated the detection of small CMBs. The reliability of this result was confirmed by the excellent inter-rater agreement for CMB counting as indicated by the high ICC metrics. This result was not surprising due to the initial automated detection step [33] that was used and stresses the importance of automated detection algorithms for obtaining reliable, consistent CMB counts, especially when there is a large number of CMBs present. The ability to detect additional smaller, lower contrast CMBs is critical for accurately characterizing their initial onset and evolution over time, a distinct advantage of using a multi- rather than dual-echo sequence [26–28] for this application.

Despite its many advantages, there are several limitations in this study. To keep the TE of the first echo and total TR as short as possible, flow compensation was only performed in the readout direction in our multi-echo sequence. Typically, when flow is not compensated in the phase-encoding directions, signal dropout and displacement of vessels results, especially

for large arteries with fast flow.[27] However, we did not observe these artifacts and were more interested in the appearance of smaller vessels that are most sensitive to ionizing radiation and exhibit slow flow. This resulted in, if any, only minor signal dropout and displacement. In addition, the higher bandwidth of the multi-echo sequence further minimized these artifacts. To minimize the saturation effect of a large slab thickness, extended slab overlap was used in our sequence, which increased total scan time. However, it provided an additional advantage of mitigating some residual wrapping of the scalp in the superior slab. Our data analysis was limited by our definition of CNR, as more traditional methods to measure CNR were no longer valid after implementation of parallel imaging, phase mask filtering, minimum or maximum intensity projection, and averaging. However, our calculation of CNR, where each ROI was defined on the same region for both multi- and single-echo images, followed the definition used by several prior studies that performed similar analyses of CNR on SWI images.[34,40] In addition, to account for spatial variations due to parallel imaging, several sets of vessels from each patient were uniformly selected throughout various brain locations and median instead of mean values were calculated to account for possible intensity inhomogeneity within vessel ROIs. All of the above considerations should make our approach to measure CNR a feasible one in practice. Despite the inherent limitation of resolution on the detection of microvessels and capillaries that directly lead to the formation of an observed CMB, identifying RT-induced vascular injury on neighboring, slightly larger vascular beds surrounding CMBs is still beneficial in understanding the mechanism of vascular injury. Although we quantified the CNR of small vessels, our ability to characterize vasculopothy in this study was also limited due to the lack of a reference standard from catheter or CT angiography in these patients. Having a reference and larger patient sample size would determine the influence of CNR variation on the measurement of continuity and size of small distal vessels.

Conclusions

In conclusion, a 3D gradient echo sequence with four echoes for the simultaneous acquisition of TOF-MRA and SWI images was successfully implemented at 7T. The resulting image quality obtained from the multi-echo sequence was comparable to the corresponding single-echo sequences for the depiction of both arteries and veins, and improved CMB detection. The merging of these objects on one image without the need for registration will ultimately facilitate the quantification of metrics that can characterize the mechanisms of radiation-induced vascular injury as well as other neurologic disorders where CMBs are present such as CAA, stroke, TBI, and Alzheimer's disease.

Acknowledgments

References

1. Laperriere N, Zuraw L, Cairncross G. Radiotherapy for newly diagnosed malignant glioma in adults: a systematic review. Radiother Oncol. 2002; 64:259–273. [PubMed: 12242114]

2. Valk PE, Dillon WP. Radiation-injury of the brain. AJNR Am J Neuroradiol. 1991; 12:45–62. [PubMed: 7502957]

3. Jain R, Robertson PL, Gandhi D, Gujar SK, Muraszko KM, Gebarski S. Radiation-induced cavernomas of the brain. AJNR Am J Neuroradiol. 2005; 26:1158–1162. [PubMed: 15891176]

4. Ullrich NJ, Robertson R, Kinnamon DD, et al. Moyamoya following cranial irradiation for primary brain tumors in children. Neurology. 2007; 68:932–938. [PubMed: 17372129]

5. Omura M, Aida N, Sekido K, Kakehi M, Matsubara S. Large intracranial vessel occlusive vasculopathy after radiation therapy in children: clinical features and usefulness of magnetic resonance imaging. Int J Radiat Oncol Biol Phys. 1997; 38:241–249. [PubMed: 9226309]

6. Fajardo LF. The pathology of ionizing radiation as defined by morphologic patterns. Acta Oncol. 2005; 44:13–22. [PubMed: 15848902]

7. Fazekas F, Kleinert R, Roob G, et al. Histopathologic analysis of foci of signal loss on gradient-echo T2*-weighted MR images in patients with spontaneous intracerebral hemorrhage: evidence of microangiopathy-related microbleeds. AJNR Am J Neuroradiol. 1999; 20:637–642. [PubMed: 10319975]

8. Lupo JM, Chuang CF, Chang SM, et al. 7-Tesla susceptibility-weighted imaging to assess the effects of radiotherapy on normal-appearing brain in patients with glioma. Int J Radiat Oncol Biol Phys. 2012; 82:e493–e500. [PubMed: 22000750]

9. Zeng Q, Kang X, Li C, Zhou G. Detection of hemorrhagic hypointense foci in radiation injury region using susceptibility-weighted imaging. Acta Radiol. 2011; 52:115–119. [PubMed: 21498336]

10. Tanino T, Kanasaki Y, Tahara T, et al. Radiation-induced microbleeds after cranial irradiation: evaluation by phase-sensitive magnetic resonance imaging with 3.0 tesla. Yonago Acta Med. 2013; 56:7–12. [PubMed: 24031146]

11. Lupo, JM.; Anwar, M.; Hess, CP.; Chang, SM.; Nelson, SJ. Relating radiation dose to microbleed formation in patients with glioma; Proceedings of the 20th Annual Meeting of ISMRM, Melbourne; 2012; abstract 186

12. Greenberg SM, O'Donnell HC, Schaefer PW, Kraft E. MRI detection of new hemorrhages: potential marker of progression in cerebral amyloid angiopathy. Neurology. 1999; 53:1135–1138. [PubMed: 10496283]

13. Werring DJ, Coward LJ, Losseff NA, Jager HR, Brown MM. Cerebral microbleeds are common in ischemic stroke but rare in TIA. Neurology. 2005; 65:1914–1918. [PubMed: 16380612]

14. Goos JD, Kester MI, Barkhof F, et al. Patients with Alzheimer disease with multiple microbleeds: relation with cerebrospinal fluid biomarkers and cognition. Stroke. 2009; 40:3455–3460. [PubMed: 19762705]

15. Scheid R, Preul C, Gruber O, Wiggins C, von Cramon DY. Diffuse axonal injury associated with chronic traumatic brain injury: evidence from T2*-weighted gradient-echo imaging at 3 T. AJNR Am J Neuroradiol. 2003; 24:1049–1056. [PubMed: 12812926]

16. Werring DJ, Gregoire SM, Cipolotti L. Cerebral microbleeds and vascular cognitive impairment. J Neurol Sci. 2010; 299:131–135. [PubMed: 20850134]

17. Ayaz M, Boikov AS, Haacke EM, Kido DK, Kirsch WM. Imaging cerebral microbleeds using susceptibility weighted imaging: one step toward detecting vascular dementia. J Magn Reson Imaging. 2010; 31:142–148. [PubMed: 20027582]

18. Greenberg SM, Vernooij MW, Cordonnier C, et al. Cerebral microbleeds: a guide to detection and interpretation. Lancet Neurol. 2009; 8:165–174. [PubMed: 19161908]

19. Nandigam RNK, Viswanathan A, Delgado P, et al. MR imaging detection of cerebral microbleeds: effect of susceptibility-weighted imaging, section thickness, and field strength. AJNR Am J Neuroradiol. 2009; 30:338–343. [PubMed: 19001544]

20. Reichenbach JR, Venkatesan R, Schillinger DJ, Kido DK, Haacke EM. Small vessels in the human brain: MR venography with deoxyhemoglobin as an intrinsic contrast agent. Radiology. 1997; 204:272–277. [PubMed: 9205259]

21. Nishimura DG. Time-of-flight MR angiography. Magnet Reson Med. 1990; 14:194–201.

22. von Morze C, Xu D, Purcell DD, et al. Intracranial time-of-flight MR angiography at 7T with comparison to 3T. J Magn Reson Imaging. 2007; 26:900–904. [PubMed: 17896360]

23. von Morze C, Purcell DD, Banerjee S, et al. High-resolution intracranial MRA at 7T using autocalibrating parallel imaging: initial experience in vascular disease patients. Magn Reson Imaging. 2008; 26:1329–1333. [PubMed: 18508216]

24. Parker DL, Yuan C, Blatter DD. MR angiography by multiple thin slab 3D acquisition. Magn Reson Med. 1991; 17:434–451. [PubMed: 2062215]

25. Du YPP, Jin ZY, Hu YZ, Tanabe J. Multi-echo acquisition of MR angiography and venography of the brain at 3 Tesla. J Magn Reson Imaging. 2009; 30:449–454. [PubMed: 19629975]

26. Du YPP, Jin ZY. Simultaneous acquisition of MR angiography and venography (MRAV). Magn Reson Med. 2008; 59:954–958. [PubMed: 18429022]

27. Deistung A, Dittrich E, Sedlacik J, Rauscher A, Reichenbach JR. ToF-SWI: simultaneous time of flight and fully flow compensated susceptibility weighted imaging. J Magn Reson Imaging. 2009; 29:1478–1484. [PubMed: 19472425]

28. Bae KT, Park SH, Moon CH, Kim JH, Kaya D, Zhao T. Dual-echo arteriovenography imaging with 7T MRI. J Magn Reson Imaging. 2010; 31:255–261. [PubMed: 20027596]

29. Brau AC, Beatty PJ, Skare S, Bammer R. Comparison of reconstruction accuracy and efficiency among autocalibrating data-driven parallel imaging methods. Magn Reson Med. 2008; 59:382–395. [PubMed: 18228603]

30. Haacke EM, Lindskog ED, Lin W. A fast, iterative, partial-Fourier technique capable of local phase recovery. J Magn Reson. 1991; 92:126–145.

31. Roemer PB, Edelstein WA, Hayes CE, Souza SP, Mueller OM. The NMR phased-array. Magn Reson Med. 1990; 16:192–225. [PubMed: 2266841]

32. Smith SM. Fast robust automated brain extraction. Hum Brain Mapp. 2002; 17:143–155. [PubMed: 12391568]

33. Bian W, Hess CP, Chang SM, Nelson SJ, Lupo JM. Computer-aided detection of radiation-induced cerebral microbleeds on susceptibility-weighted MR images. Neuroimage Clin. 2013; 2:282–290. [PubMed: 24179783]

34. Denk C, Rauscher A. Susceptibility weighted imaging with multiple echoes. J Magn Reson Imaging. 2010; 31:185–191. [PubMed: 20027586]

35. Conijn MM, Geerlings MI, Luijten PR, et al. Visualization of cerebral microbleeds with dual-echo T2*-weighted magnetic resonance imaging at 7.0 T. J Magn Reson Imaging. 2010; 32:52–59. [PubMed: 20578010]

36. Theysohn JM, Kraff O, Maderwald S, et al. 7 Tesla MRI of microbleeds and white matter lesions as seen in vascular dementia. J Magn Reson Imaging. 2011; 33:782–791. [PubMed: 21448941]

37. de Bresser J, Brundel M, Conijn MM, et al. Visual cerebral microbleed detection on 7T MR imaging: reliability and effects of image processing. AJNR Am J Neuroradiol. 2013; 34:E61–E64. [PubMed: 22345502]

38. Brainovich V, Sabatini U, Hagberg GE. Advantages of using multiple-echo image combination and asymmetric triangular phase masking in magnetic resonance venography at 3 T. Magn Reson Imaging. 2009; 27:23–37. [PubMed: 18599241]

39. Gilbert G, Savard G, Bard C, Beaudoin G. Quantitative comparison between a multiecho sequence and a single-echo sequence for susceptibility-weighted phase imaging. Magn Reson Imaging. 2012; 30:722–730. [PubMed: 22459441]

40. Feng W, Neelavalli J, Haacke EM. Catalytic multiecho phase unwrapping scheme (CAMPUS) in multiecho gradient echo imaging: removing phase wraps on a voxel-by-voxel basis. Magn Reson Med. 2013; 70:117–126. [PubMed: 22886762]
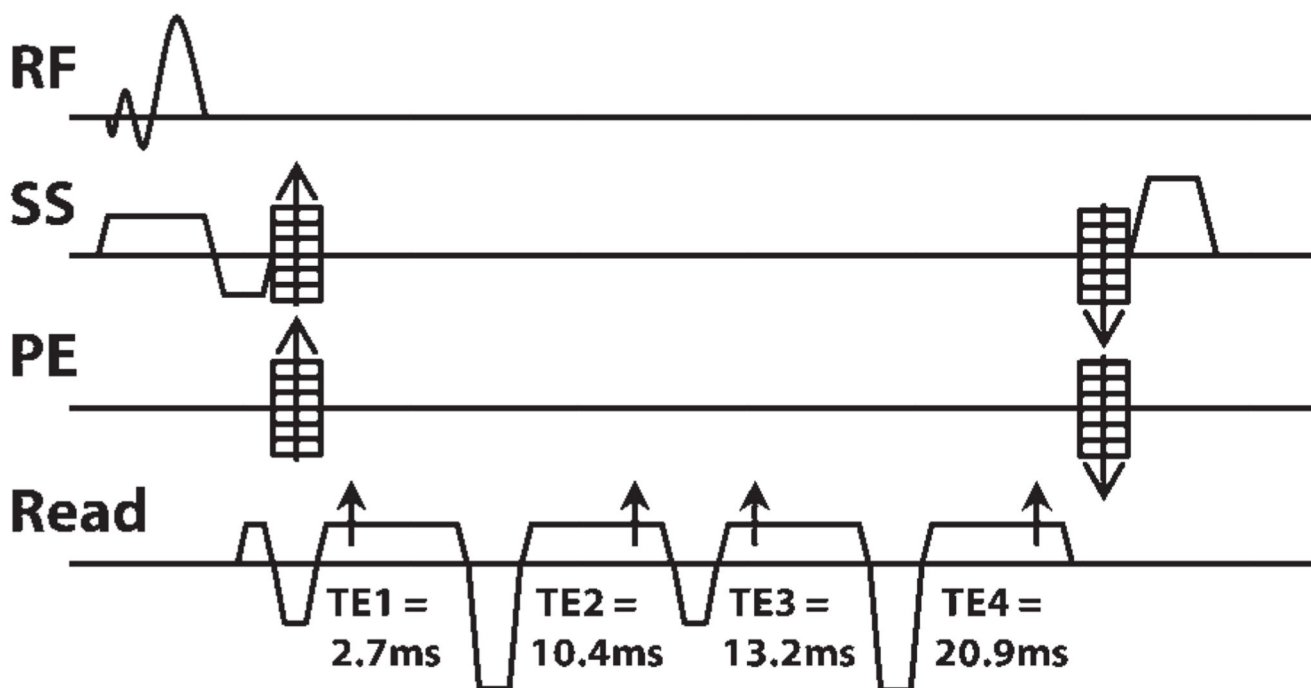
FIGURE 1. The diagram of the proposed 3D multi-echo spoiled gradient echo sequence. The sequence contains 4 partially acquired (65%) echoes at the TEs (*arrows*) of 2.7, 10.4, 13.2, and 20.9 ms. The data from the first echo are used to generate TOF-MRA, while the data from the remaining 3 echoes are combined to generate SWI images. Flow compensation was performed only in the readout direction using a prewind bipolar gradient for the first echo and flyback gradients for the other 3 echoes. (RF: rf pulse; SS: Slice selection gradient; PE: Phase encoding gradient)
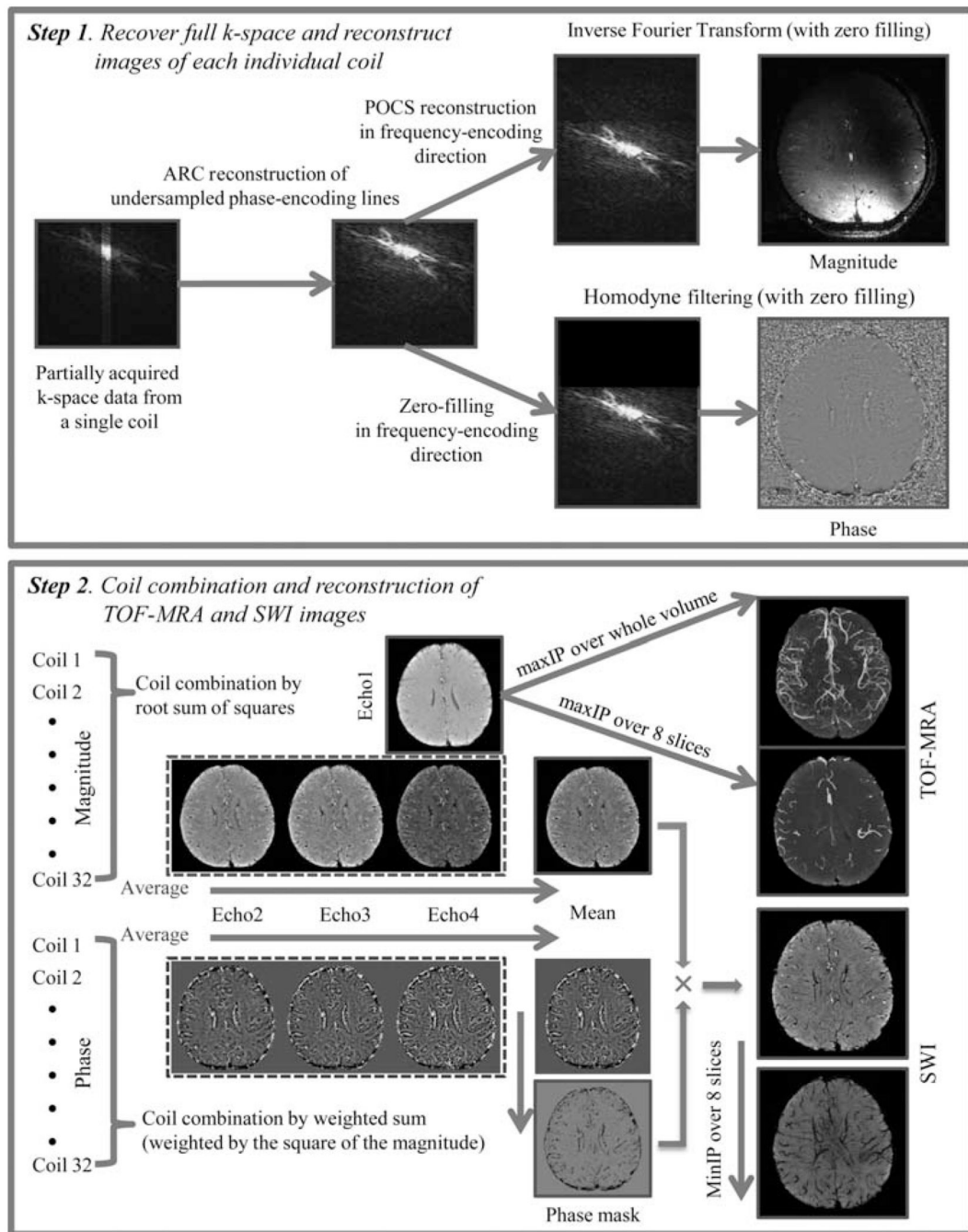
FIGURE 2. Image reconstruction and postprocessing pipelines for TOF-MRA and SWI images acquired from the multi-echo sequence
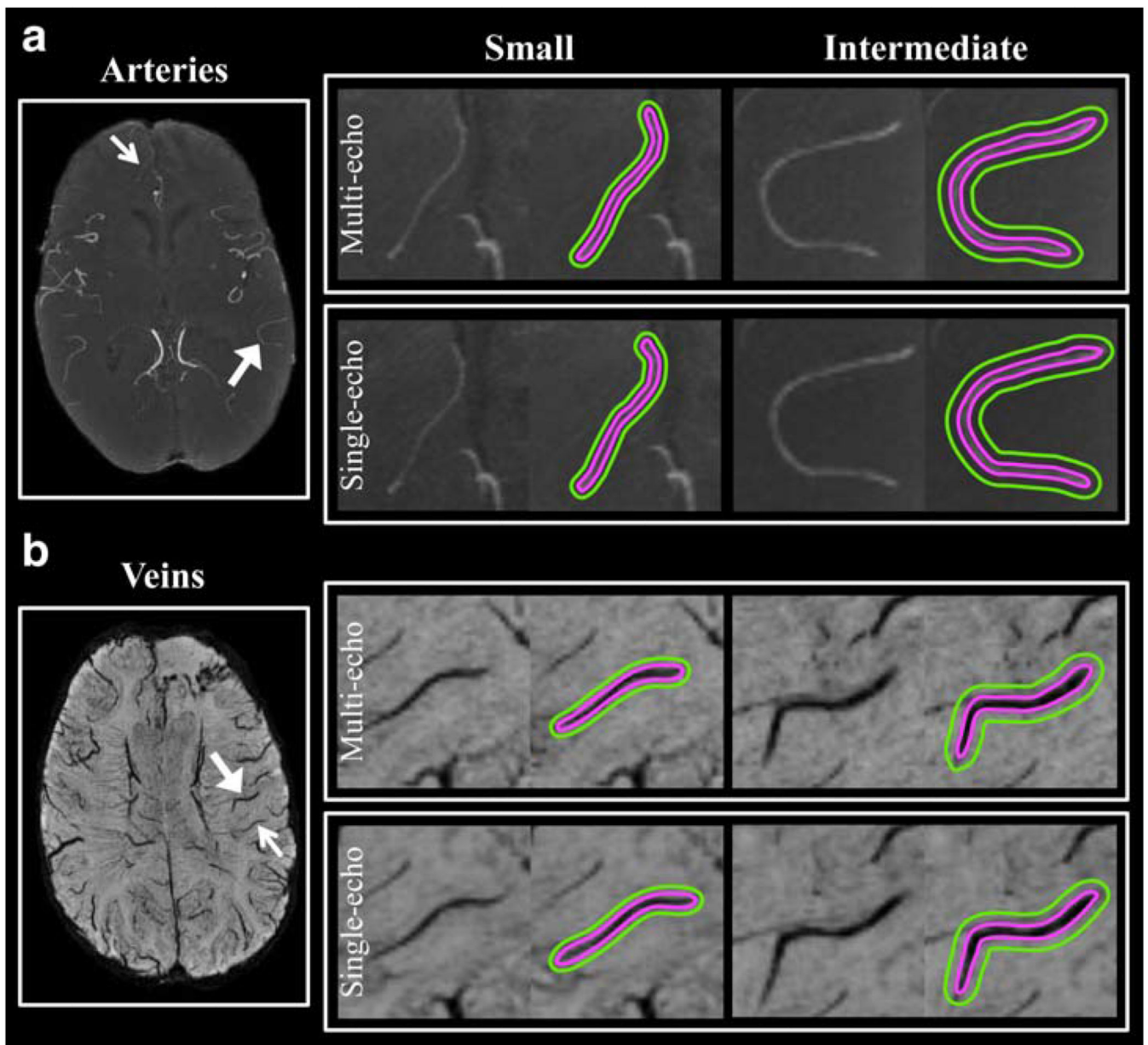
FIGURE 3. ROIs of veins and arteries were defined on TOF-MRA (A) and SWI (B) images, which were maximally and minimally projected over 8mm thickness, respectively. ROIs were paired between the multi-echo images (*top rows* in A & B) and corresponding single-echo images (*bottom rows* in A & B). Each vessel ROI (*pink*) was dilated (*green*) to create a corresponding background tissue ROI after subtracting out the original vessel ROI. The ROIs were defined for *intermediate* diameter (between 1 and 2 mm, *large arrows*) and *small* diameter (less than 1 mm, *small arrows*) arteries and veins
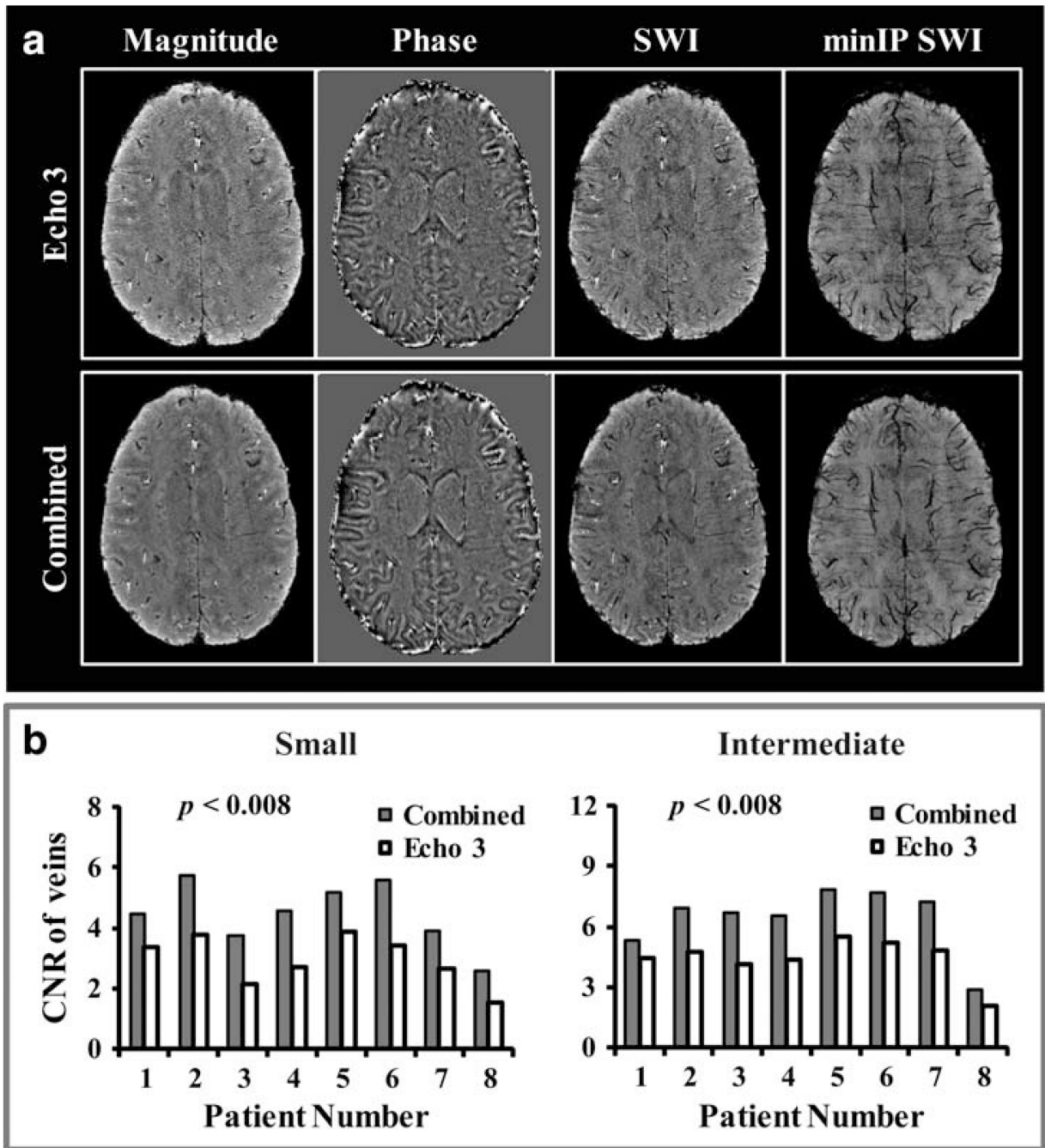
FIGURE 4. A: Magnitude, phase, SWI, and minIP images from echo 3 (*top row*) and combined processing (*bottom row*), where both magnitude and phase images from echoes 2 to 4 were first created individually and then averaged to generate mean magnitude and phase images before generating the final SWI images. The SNR was greatly improved for the combined composite SWI image compared with that from the echo 3 (whose TE was similar to that of single-echo SWI sequence), which is evident by a more homogeneous display of the ventricles on the former. B: Plots of average CNR for both *small* and *intermediate* veins from minIP SWI images of echo 3 and the composite SWI image for all 8 patients. The composite SWI image had significantly higher CNR for both vein sizes in all patients
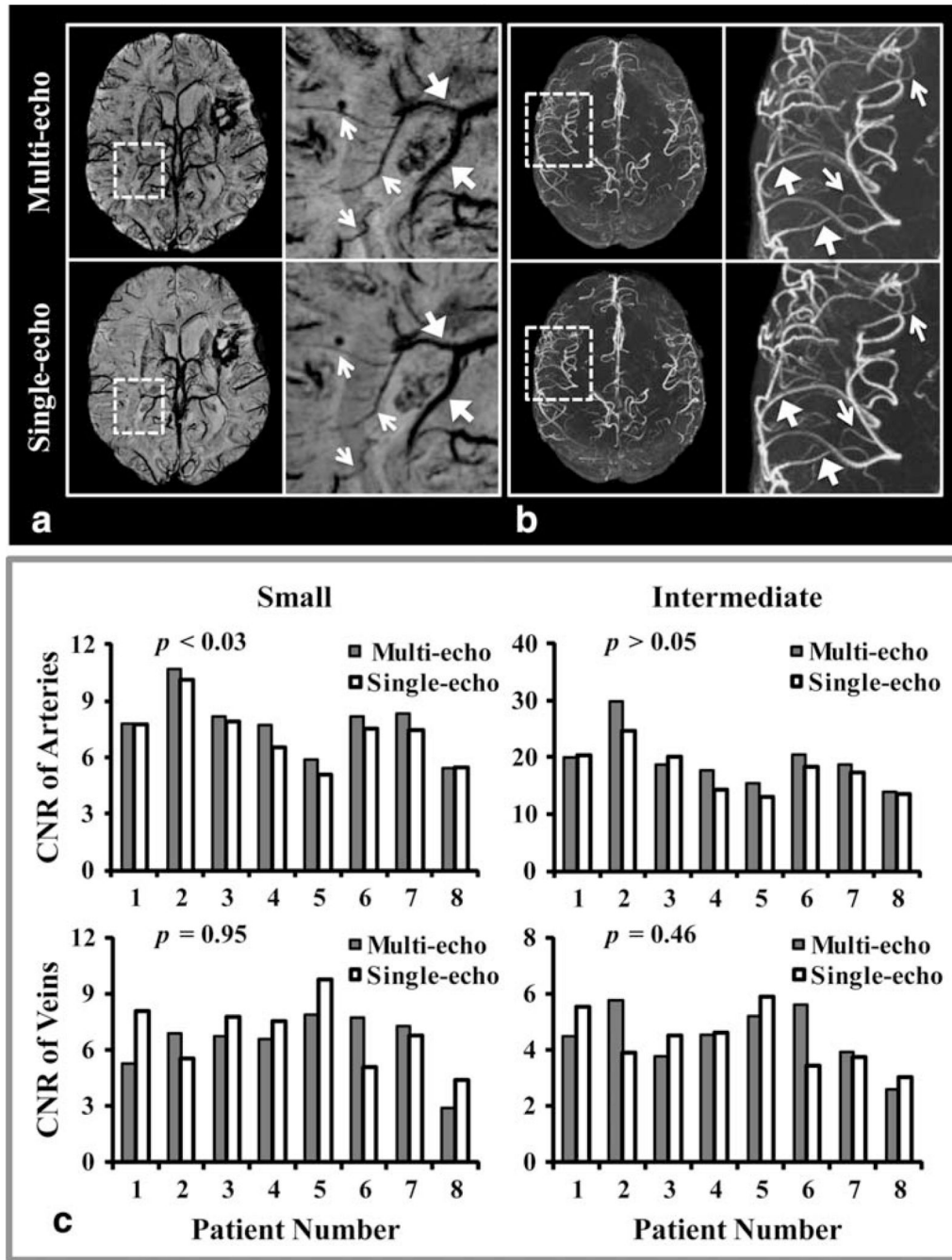
FIGURE 5. The minIP SWI (A) and maxIP TOF-MRA (B) for both multi-echo and individual single-echo sequences. For illustration purposes, a local region (*dashed-box*) from each is zoomed in and shown on the right column. On (A), single-echo SWI better delineates larger veins (*large arrows*) because of its high CNR, while multi-echo SWI better illustrates smaller veins and CMBs primarily due to its higher slice resolution. On (B), all arteries including both larger (*large arrows*) and smaller (*small arrows*) arteries have similar contrast on both multi- and single-echo TOF-MRA, despite the slightly worse background suppression of the multi-echo acquisition due to a longer TR. C: Plots of average CNR for each type of vessel from all 8 patients' images acquired from both multi- and single-echo sequences. Except for *small* arteries, which had a slightly significantly higher CNR on TOF-MRA from the multi-echo sequence, all other vessels had comparable CNRs between images from the multi- and single-echo sequences
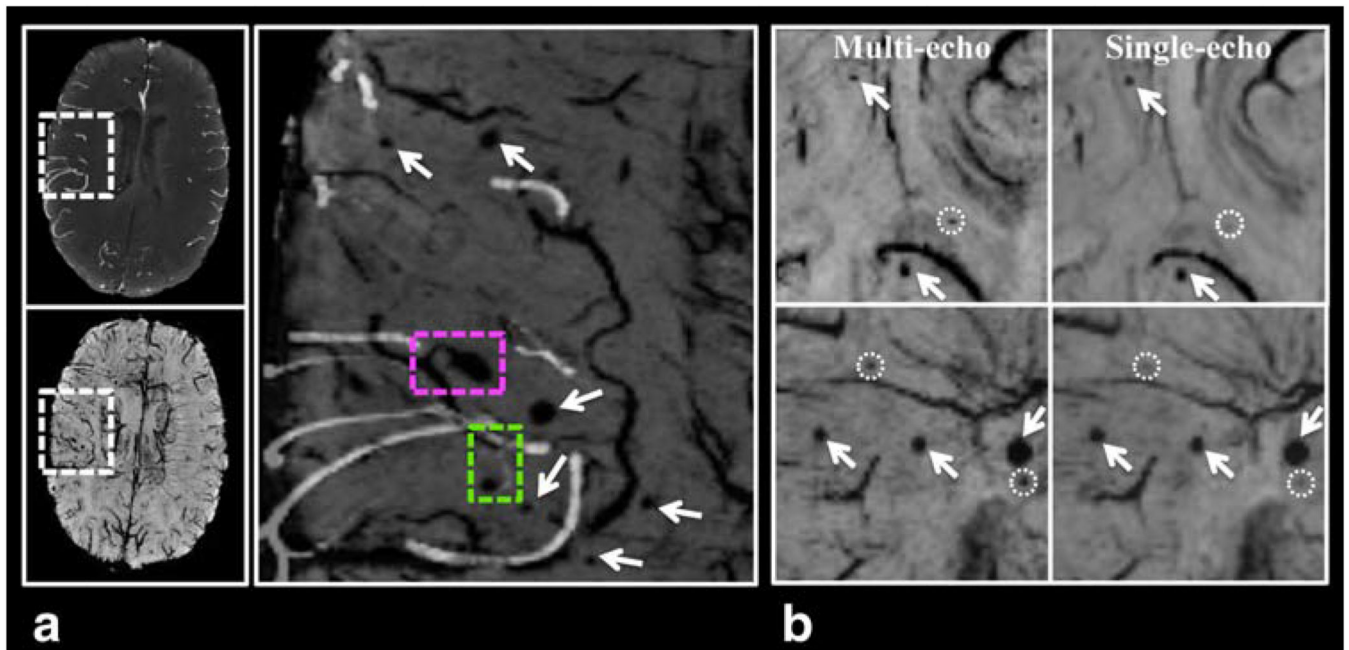
FIGURE 6. Benefits from using the multi-echo sequence. A: The multi-echo sequence allows arteries from TOF-MRA images (maxIP over 8 mm) to be overlaid on CMBs and veins from minIP SWI images without the need for registration. From the overlaid image (zoomed in to a local region specified by the dashed-box on the original images) on the left column, it can be clearly seen that one CMB is arising from venous vessels (*pink dashed-box*) while another one appears to originate from arterioles (*green dashed-box*). B: minIP SWI Images from two different patients (*top* and *bottom rows*) showing CMBs (*arrows*) that are visualized on both single- and multi-echo images, and three additional CMBs that are only detected on multi-echo SWI (*dashed-circles*)

TABLE 1

Acquisition Parameters for Single- and Multi-echo Sequences[a]

	3D SWI	3D TOF-MRA	3D Multi-echo MRA/SWI
Slice thickness	2 mm	1 mm	1 mm
Slab thickness	1 slab	3 slabs	3 slabs
	36 slice	30 slices/slab	36 slices /slab
		6 overlapping slices	12 overlapping slices
Bandwidth	15.25 kHz	41.76 kHz	41.76 kHz
K-Space coverage	Full	Partial (65%)	Partial (65%)
TR	50 ms	30 ms	40 ms
TE(s)	16 ms	2.7 ms	2.7, 10.5, 13.2, 20.9 ms
Acquisition time	4 mins/50 s	6 mins/40 s	10 mins/36 s

[a]Parameters that are the same to all 3 sequences: FOV 24 cm, flip angle 25°, acquisition matrix 512 × 384, in-plane resolution 0.46 × 0.63 mm^2, and acceleration factor 3.

TABLE 2

Number of CMBs Detected on minIP SWI Images From Both Single- and Multi-echo Sequences

Patients	Single-echo			Multi-echo		
	Rater1	Rater2	Average	Rater1	Rater2	Average
1	330	317	323.5	372	364	368
2	36	26	31	44	31	37.5
3	28	11	19.5	42	29	35.5
4	35	28	31.5	53	48	50.5
5	22	10	16	30	12	21
6	83	72	77.5	99	78	88.5
7	228	224	226	271	269	270
8	70	77	73.5	75	74	74.5
Total	832	765	798.5	986	902	945.5